# Multifaceted spectroscopic study of electrical and optical properties in sodium manganese oxide ceramics

Marwa Krichen, Narimen Chakchouk, Ebtehal Elghmaz, Fadhel Hajlaoui, Karim Karoui

# Multifaceted Spectroscopic Study of Electrical and Optical Properties in Sodium Manganese Oxide Ceramics

**Marwa Krichen [a], Narimen Chakchouk [a], Ebtehal Elghmaz [b], Fadhel Hajlaoui [c]. Karim Karoui [a,d]**

[a] *Laboratory of Spectroscopic and Optical Characterization of Materials, Faculty of Sciences of Sfax, University of Sfax, B.P. 1171, 3000 Sfax, Tunisia.*

[b] *Department of Physics, King Khalid University, Abha 61421, Saudi Arabia.*

[c] *Laboratory of Solid State Physico-Chemistry, Department of Chemistry, Faculty of Sciences of Sfax, University of Sfax, B.P. 1171, 3000 Sfax, Tunisia*

[d] *GREMAN UMR 7347-CNRS, CEA, INSACVL, University of Tours, Blois, France*

[*] *Corresponding author. E-mail address: karim.karoui@fss.usf.tn*

*Tel: 0033782426685*

## Abstract

$NaMn_2O_4$ ceramic was successfully synthesized via a high-temperature solid-state reaction. Its structural, optical, and electrical transport properties were comprehensively investigated. Rietveld refinement of X-ray diffraction data confirmed that the compound crystallizes in the orthorhombic system with the Pnam space group. Optical measurements using UV–Vis spectroscopy revealed a direct band gap of approximately 2.64±0.002 eV, confirming the semiconducting nature of $NaMn_2O_4$ and suggesting its suitability for optoelectronic and energy-related applications. Electrical characterization was carried out using impedance spectroscopy over a frequency range of 1 Hz to 1 MHz and a temperature range of 303–423 K. The AC conductivity was analyzed using Jonscher's power law, and the conduction mechanism was found to follow the Overlapping Large Polaron Tunneling (OLPT) model. This indicates that ionic transport occurs via thermally activated hopping of $Na^+$ ions along the [001] tunnel direction, while electronic conduction is facilitated by electron hopping between $Mn^{3+}$ and $Mn^{4+}$.

*Keywords: impedance spectroscopy, conductivity, gap energy, conduction mechanisms*

## I. Introduction

The increasing need to integrate renewable energy sources and advance electric mobility has driven intensive research into energy storage solutions that are efficient, cost-effective, and environmentally sustainable. Among the different storage technologies, rechargeable batteries have gained particular attention due to their high energy density, portability, and technological maturity. High-energy storage systems are essential in a wide range of applications, including

portable electronic devices (such as laptops and mobile phones), electric vehicles (both hybrid and fully electric), and renewable energy infrastructures like wind turbines and solar panels. In this context, Sodium-ion batteries (SIBs) have emerged as a promising alternative to lithium-ion batteries (LIBs), particularly for large-scale applications, thanks to the wide availability, low cost, and environmental advantages of sodium resources [1].

When the Exxon Research and Engineering Company first suggested using sodium ions as intercalating species in rechargeable batteries in 1980, the path toward sodium-based energy storage got underway [2–3]. Ever since, a lot of work has gone into creating appropriate electrode materials, poly-anionic compounds [4], NASICON-type structures [5] and including layered transition metal oxides [6].

A key aspect in the development of sodium-ion batteries (SIBs) is the design of electrode materials that combine high specific capacity, good cycling stability, and fast charge–discharge performance. In this context, manganese-based oxides stand out as promising candidates thanks to their low cost, environmental compatibility, and the ability of manganese to exhibit multiple oxidation states ($Mn^{3+}/Mn^{4+}$). This redox flexibility allows for efficient and reversible ion intercalation processes, which are essential for high electrochemical performance.

Various manganese-based compounds, including $LiMn_2O_4$, $MgMn_2O_4$, $ZnMn_2O_4$, $CaMn_2O_4$ and $NaMn_2O_4$…, have been widely investigated due to their structural robustness, favorable electrochemical properties, and versatility across different energy storage systems. These materials benefit from the combination of electronic conductivity and ionic mobility, both of which are critical for improving charge transport mechanisms. [7-9]

In this work, particular attention is given to $NaMn_2O_4$, which merges the advantages of sodium-based chemistry and manganese-based redox activity. Owing to its tunnel or layered framework and mixed $Mn^{3+}/Mn^{4+}$ valence states, $NaMn_2O_4$ demonstrates effective sodium ion storage and mobility. Its structural and conductive properties play a pivotal role in enhancing sodium diffusion and overall cell performance. For example, in the well-studied $LiMn_2O_4$ spinel, the equal distribution of $Mn^{3+}$ and $Mn^{4+}$ ions lead to an average oxidation state of +3.5. The presence of $Mn^{3+}$ can induce Jahn–Teller distortions, affecting the crystal structure and, consequently, the transport properties of the material. Understanding these structural effects is fundamental to improving manganese-based cathodes for next-generation SIBs.

The compound $NaMn_2O_4$ has previously been investigated by J. Akimoto and al. [10], and was reported to crystallize in the orthorhombic system with a space group P*nam*. The refined lattice parameters are $a$ = 8.9055 Å, $b$ = 11.0825 Å, and $c$ = 2.8524 Å, with a unit cell volume $V$ = 281.52 Å$^3$ and Z = 4. While the earlier study mainly addressed structural characteristics,

the present work also explores the morphological, optical, electrical, and dielectric properties in order to identify the conduction mechanism of the compound and to study the optoelectronic performance of this material.

## II. Experimental procedure

### II.1. Synthesis procedure

$NaMn_2O_4$ ceramic was synthesized using the conventional solid-state reaction route from stoichiometric amounts of $Na_2CO_3$ and $MnO_2$ powders (both 99.9% purity, Sigma-Aldrich), according to the reaction:

$$2\,Na_2CO_3 + 8\,MnO_2 \rightarrow 4\,NaMn_2O_4 + 2\,CO_2 + O_2$$

The weighed powders were thoroughly mixed via ball-milling with 250 tr/min for 2 hours to reduce particle size and improve the homogeneity and reactivity of the precursor mixture. The resulting powder was then preheated to 623 K for 12 hours. To further promote the solid-state reaction, the calcinated powder was pressed into pellets with a diameter of 8 mm using uniaxial pressure. Finally, the obtained cylindrical $NaMn_2O_4$ pellets were sintered at 1123 K for 12 hours an air atmosphere to weld the grains and improve the density of the material.

### II.2. Material characterization

To determine crystal structure and phase purity of the synthesized compound, powder X-ray diffraction (XRD) analysis was performed at room temperature using the Bruker D8 Discover Twin diffractometer with advanced Bragg–Brentano geometry with copper Kα radiation ($\lambda$ = 1.5406 Å) over a broad range of Bragg angles ($10° < 2\theta < 66°$) with a step $\Delta(2\theta) = 0.022°$. Structure refinements were carried out using the FullProf program package based on the Rietveld method. The unit cell parameters were refined using the least squares method based on the powder diffraction data. The morphology of this sample was studied by scanning microscope. The optical spectrum of the investigated compound was carried out at room temperature using a UV-3101PC scanning spectrophotometer (Integrated Sphere) in the wavelength range 200–800 nm with a resolution of 0.5 nm. For the electrical measurements, a pellet with a thickness of 1 mm and a diameter of 8 mm was used. All electrical measurements of real and imaginary components of the impedance parameters were made over a wide range of temperature (303 – 423) K and frequency range (1 Hz – 1 MHz) with an AC voltage of 1 V Soltran SI 1260 impedance analyzer. To ensure good electrical contact, the pellet surfaces were coated with a conductive silver paint.

## III. Results and discussion

### III.1.X-ray diffraction and crystal structure

The phase purity and crystal structure of the prepared sample were examined using powder X-ray diffraction (XRD) analysis **Fig. 1**. Rietveld refinement was carried out to obtain detailed structural information which is confirms the absence of impurity peaks or secondary phases and the successful synthesis of a pure, high-quality material. The $NaMn_2O_4$ sample exhibited sharp and intense diffraction peaks, indicating a high degree of crystallinity. All reflection peaks correspond to orthorhombic structure with the Pnam space group. The lattice parameters, refined using the pseudo-Voigt function to simulate peak shapes, are summarized in **Table 1** and show good agreement with literature values [10].

The atomic positional parameters were initially derived from Akimoto's work and refined using the Rietveld method. The acquisition parameters used for the measurements are also detailed in **Table 2**. The structural framework is isostructural with known calcium ferrite-type compounds such as $CaFe_2O_4$, $NaFeTiO_4$, and $NaTi_2O_4$, sharing similar coordination environments and crystallographic symmetry. **Figure 2(a)** illustrates the crystal structure projected along the c-axis, highlighting the arrangement of the framework [12].

The architecture of $NaMn_2O_4$ shows "double rutile" chains formed by edge-sharing $MnO_6$ octahedral aligned along the c-axis. Four such chains are interconnected via corner-sharing, constructing a three-dimensional network that generates one-dimensional tunnels along [001] direction, where $Na^+$ cations are located. As depicted in **Figure 2(b)**, the manganese ions occupy two distinct crystallographic sites: $Mn_1$ and $Mn_2$. The $Mn_1$–O bond lengths range from 1.883 to 2.256 Å, indicative of a Jahn–Teller distortion typically associated with $Mn^{3+}$ ions. Conversely, the $Mn_2$–O bond lengths vary between 1.516 and 2.177 Å, suggesting a more regular octahedral environment characteristic of $Mn^{4+}$ ions. This differentiation implies a mixed-valence state with an ordered distribution of $Mn^{3+}$ and $Mn^{4+}$ within the structure.

From an electronic configuration standpoint, $Mn^{3+}$ adopts a high-spin state with a configuration of $3d^4$: $t_{2g}^3 e_g^1$, which is Jahn–Teller active due to the presence of an unpaired electron in the $e_g$ orbital, causing a distortion in the $MnO_6$ octahedral. In contrast, $Mn^{4+}$ has a stable $3d^3$: $t_{2g}^3 e_g^0$ configuration, leading to a more regular octahedral geometry. Structurally, half of the $MnO_6$ octahedral are oriented along the [001] direction, while the other half are alternately pointed along the opposite [00–1] direction and are connected only via shared corners. The periodic arrangement of $Mn^{3+}$ and $Mn^{4+}$ ions, combined with the Jahn–Teller distortion associated with $Mn^{3+}$, would significantly influence both electronic transport and $Na^+$ ionic mobility within the tunnel-like structure of $NaMn_2O_4$.

The tunnels contain sodium ions that are arranged in bicapped trigonal prisms ($NaO_8$) by coordination of eight oxygen atoms, with Na–O distances ranging from 2.051 to 2.757 Å. Calcium ferrite-type structures are characterized by this coordinating environment. While $NaMn_2O_4$ shares structural similarities with $CaMn_2O_4$, notable differences exist in the connectivity of the double chains and the orientation of Jahn–Teller distortions. In $CaMn_2O_4$, double chains are linked through two edges and two corners, with Jahn–Teller distortions oriented differently compared to $NaMn_2O_4$. These unique structural features of $NaMn_2O_4$, including its one-dimensional $Na^+$ diffusion pathways, distinct $Mn^{3+}/Mn^{4+}$ valence ordering, and specific sodium coordination, underscore its potential as a promising cathode material for sodium-ion battery applications [13-19].

### III.2. SEM

The structural morphology and particle size of electrode materials are key factors influencing $Na^+$ ion insertion and extraction in rechargeable sodium-ion batteries.
To evaluate these characteristics, Scanning Electron Microscopy (SEM) was used to examine the surface morphology and particle size distribution of the $NaMn_2O_4$ compound.

As shown in **Figure 3.a**, the SEM image of the synthesized $NaMn_2O_4$ compound reveals that the material is composed of micrometer-sized particles with a quasi-spherical shape and a broad size distribution. The microstructure exhibits visible porosity, and a clear tendency toward particle agglomeration is observed, which could hinder ion transport and thereby affect the material's conductivity and electrochemical performance.

To further analyze the grain size distribution, the Image J software was employed to statistically evaluate the sizes of numerous individual particles from the SEM images. The resulting histogram, presented in **Figure 3.b**, indicates that the particles follow a Gaussian distribution, with an average size of approximately 1.011±0.025 μm**.** This average particle size is larger than that of $LiMn_2O_4$, which was previously reported to be around 0.13 μm [11]. Despite the aggregation observed, the relatively small particle size in $NaMn_2O_4$ remains advantageous for reducing ion diffusion paths, potentially improving charge storage behavior [20, 21].

### III.3. Optical characterization

To investigate the optical behavior of $NaMn_2O_4$, the solid-state UV–visible spectroscopy was carried out and presents the experimental absorption spectrum recorded at room temperature **Figure 4 (a)**. This spectrum reveals four distinct absorption bands centered at approximately 258 nm, 316 nm, 402 nm, and 532 nm, indicating multiple electronic transitions within the crystal lattice. The broad absorption band observed near 532 nm is attributed to electronic

transitions from the valence band to the conduction band. This process mainly involves the Mn 3d orbitals, with additional contributions from the O 2p states. Such a transition is typically linked to intervalence charge transfer between $Mn^{3+}$ and $Mn^{4+}$ ions, reflecting the mixed-valence nature of the compound. The absorption band observed at 402 nm is attributed to intra-atomic d–d transitions within the distorted $Mn^{3+}$ octahedral ($t_2g^3$ $eg^1$), which are weakly allowed due to the Jahn–Teller distortion breaking the Centro-symmetry of the site. The peak at 316 nm likely corresponds to ligand-to-metal charge transfer transition, involving the transfer of electrons from the oxygen 2p orbitals to the manganese 3d orbitals ($Mn^{3+}$), influenced by the presence of the Jahn–Teller active $Mn^{3+}$ ions. Finally, the sharp absorption band at 258 nm is primarily attributed to charge transfer transitions from oxygen 2p orbitals to the 3d orbitals of $Mn^{4+}$, reflecting the strong interaction between oxygen and manganese atoms in the octahedral framework. These findings highlight the complex electronic environment within $NaMn_2O_4$, dominated by mixed valence states, local distortions, and strong metal–oxygen covalence, which define the semiconducting nature and optical characteristics of the material [11, 22-25].

- **Direct optical band gap**

The determination of the optical band gap energy (Eg) is very important for the comprehension of the electronic material properties. Among different procedures that have been proposed, the most adequate procedure to powder compounds is the application of the Tauc relation combined with the Kubelka–Munk function. This relation is given by the following expression:

$$(\boldsymbol{\alpha h\nu})^{1/n} = \boldsymbol{B}(\boldsymbol{h\nu} - \boldsymbol{E_g}) \qquad (1)$$

The analysis of optical absorption data relies on several essential parameters:

- ✓ **Photon energy (hν):** Refers to the energy carried by the absorbed light.
- ✓ **Optical band gap (Eg):** It is the valence-conduction band gap, significant to account for the electronic transitions of the material.
- ✓ **Band tailing parameter (B)**: A coefficient characterizing the density and distribution of localized states in the band gap.
- ✓ **Absorption coefficient (α)**: Defines the intensity at which the material absorbs light at a specific wavelength.
- ✓ **Transition exponent (n)**: Determines whether the electronic transition is direct or indirect.

For treatment of reflectance data for powdered or opaque materials, the Kubelka–Munk model is generally used. This model connects the absorption coefficient (α) with measured reflectance (R) and its wavelength dependence, allowing for precise calculation of optical

properties. Here, α is the absorption coefficient, and (hν) represents the incident photon energy, which can be calculated using the following relation [26]:

$$\boldsymbol{h\nu\ (eV) = \frac{1240}{\lambda(cm)}} \qquad (2)$$

The Kubelka–Munk function F(R) is given by the following formula:

$$\boldsymbol{F(R) = (1-R)^2/2R} \qquad (3)$$

R corresponds to the diffuse reflectance, B is a constant independent of photon energy known as the band tailing parameter, α denotes the absorption coefficient, $E_g$ represents the optical band gap energy, and n is an exponent that characterizes the nature of the electronic transition between the valence and conduction bands—where n = 1/2 corresponds to an allowed direct transition, and n = 2 corresponds to an allowed indirect transition.

In **figure 4 (b)**, a graph of $(\alpha h\nu)^2$ as a function of photon energy (hν) is depicted. The optical band gap ($E_g$) for direct transitions is estimated by extrapolating the linear portion of the curves to intersect (hν) and equal 2.64±0.002 eV. This value is comparable to those observed in spinel-structured materials such as $LiMn_2O_4$ (2.57 eV), $ZnMn_2O_4$ (2.5 eV), and $NiMn_2O_4$ (2.6 eV), confirming the semiconducting nature of $NaMn_2O_4$ and highlighting its potential applicability in optoelectronic, photoelectric and energy storage devices [27].

- **Determination of Urbach energy Eu**

The Urbach energy $E_u$, which arises from phonon interactions and structural disorder, is a key parameter used to characterize disordered and amorphous materials [28]. It represents the width of the exponential absorption tail linked to localized states between the valence and conduction bands. According to recent theoretical studies, the Urbach energy also reflects the tailing of the density of states near the band edges, induced by both thermal vibrations and static structural irregularities. It is considered a useful indicator of short-range structural order and the presence of localized defect states in disordered semiconductors, thus providing valuable insight into the electronic structure and the degree of disorder in the material. This parameter can be estimated using the Urbach model [29-30]. The high value of $E_u$ typically indicates a high degree of disorder, often caused by the incorporation of a large number of foreign atoms into the lattice, which leads to a narrowing of the optical band gap. Urbach energy is determined using the following expression:

$$\boldsymbol{\alpha(h\nu) = \alpha_0 exp\left(\frac{h\nu}{E_u}\right)} \qquad (4)$$

or, in its logarithmic form:

$$\boldsymbol{Ln(\alpha) = Ln(\alpha_0) + \frac{h\nu}{E_u}} \qquad (5)$$

Where α is the absorption coefficient, hν is the photon energy, $\alpha_0$ is a constant and $E_u$ is the Urbach energy.

In **Figure 4 (c)**, the variation of ln(α) as a function of photon energy is presented for our compound. The extracted Urbach energy $E_u$ is approximately 0.72 eV, indicating a high degree of structural disorder within the material. Compared to $LiMn_2O_4$ [11], which exhibits a lower Urbach energy of 0.29 eV, our compound shows a more significant degree of disorder.

- **Optical extinction**

The extinction coefficient (k) represents the amount of light absorbed and scattered per unit distance as it propagates through a material. It was calculated using the following relation [31]:

$$\boldsymbol{k = \frac{\alpha\lambda}{4\pi}} \qquad (7)$$

Where α is the absorption coefficient and λ is the wavelength.

**Figure 5 (a)** illustrates the spectral dependence of the extinction coefficient for the $NaMn_2O_4$ compound. The values of k remain relatively low, on the order of $10^{-7}$, which indicates weak optical absorption in the visible and near-infrared regions [32]. This low absorption implies minimal optical losses when light propagates through the material, thereby highlighting its semi-transparent nature and potential for optical applications.

- **Refractive index**

Accurately determining the refractive index (n) is essential for the development of optical components [33]. Since n is closely related to the reflectance (R) and the extinction coefficient (k), it can be expressed through the following relation:

$$\mathbf{n = \frac{1+R}{1-R} + \sqrt{\frac{4R}{(1-R)^2} - k^2}} \qquad (8)$$

Furthermore, the behavior of the refractive index (n) at low optical frequencies was analyzed using dispersion models. In particular, the Cauchy and Wemple–DiDomenico (WDD) models were employed to describe this variation. The Cauchy model, which is empirical in nature, is particularly suitable for transparent dielectric materials. It expresses the refractive index as a function of the wavelength according to the following expression:

$$\boldsymbol{n = n_0 + \frac{A}{\lambda^2} + \frac{B}{\lambda^4}} \qquad (9)$$

As shown in **Figure 5 (b)**, the refractive index ranges from 1.16 to 7.35. The evolution of n with respect to the wavelength was used to extract the Cauchy constants ($n_0$, A, and B) by fitting the experimental data. The obtained values are: $n_0$ = 9.077**,** A = –1.146 $\mu m^{-2}$, and B = 0.051 $\mu m^{-4}$. It is worth noting that, in the transparency region of the material, the contribution of the

B term (proportional to $\lambda^{-4}$) is very small. Thus, coefficient B can be considered negligible in this spectral range, indicating that higher-order dispersion effects have a minimal influence on the refractive index behavior. The slight deviations observed between the experimental data and the fitted curve are attributed to experimental uncertainties and to the empirical nature of the Cauchy model, which does not account for all complex optical interactions.

### III.4. Impedance spectroscopy and equivalent circuit

Complex impedance spectroscopy (CIS) is a sensitive experimental method employing a low-amplitude alternating current (AC) signal to investigate the impedance characteristics of a material. Recording impedance over a wide frequency range, the method constructs an accurate impedance spectrum, providing valuable information regarding the electrical performance of the target material. It offers valuable information on charge transfer processes, including frequency-dependent impedance, relaxation time, and the roles of grains, grain boundaries, and electrode interfaces in the material [34-36].

**Figure 6 (a, b)** presents the complex impedance spectra of $NaMn_2O_4$ compound recorded at various temperatures ranging from 303 K to 423 K, and the equivalent circuits used to fit the data. The shape of the spectra reveals a single semicircular arc, indicating that the electrical response of the material is predominantly governed by grain contributions. The absence of a second semicircular arc suggests that grain boundary contributions are negligible within the measured frequency range. The semicircular arcs' centers are located below the real axis (Z'), indicating a non-Debye relaxation mechanism and a pronounced departure from ideal Debye behavior. The Cole–Cole model, which takes into consideration a distribution of relaxation times as opposed to a single time constant, is in line with this behavior.

The Nyquist plots also exhibit a typical frequency evolution, where the frequency is lowest at the high Z' end (right side) and increases toward the origin (left side), reaching a maximum at the intersection with the imaginary axis. This frequency trend further supports the capacitive nature of the material. Additionally, the appearance of an open or depressed semicircular arc in the low-frequency region at higher temperatures indicates the increasing contribution of electrode–material interface effects.

The diameter of the semicircular arcs is observed to decrease with an increasing temperature, while the corresponding maxima shifts to lower Z'' values. This behavior reflects a significant increase in DC conductivity with temperature, consistent with thermally activated charge transport.

Impedance data fitting using ZView software yielded satisfactory results. At lower temperatures ($303\ K < T < 343\ K$), the spectra were well fitted using an equivalent circuit consisting of a

resistance ($R_1$), a capacitance ($C_1$), and a constant phase element ($CPE_1$) in parallel, accounting for non-ideal capacitive behavior. At higher temperatures (353 K < T < 423 K), the model was refined by adding a second constant phase element ($CPE_2$) in series to accurately detect the transport phenomena and interfacial contributions observed at elevated temperatures [37].

A substantial agreement can be observed in **figure 6 (a, b)** between the experimental (symbol) and simulated/fitted (black lines) curves by employing the proposed circuit for different temperatures confirming that the chosen equivalent circuit describes the electric behavior of our developed compound.

The impedance of the CPE, also described as a fractal capacitive element, is defined via:

$$\boldsymbol{Z^*_{CPE} = \frac{1}{Q(j\omega)^{\alpha}}} \qquad (10)$$

where j is the imaginary unit ($j^2 = -1$) and ω the angular frequency ($\omega = 2\pi f$, f being the frequency), Q a constant independent of frequency, and α a dimensionless parameter ranging between zero and unity. The term "fractal" refers to the non-ideal capacitive behavior of the CPE, often associated with surface roughness, inhomogeneities, or a distribution of relaxation times. This latter quantifies the degree of deviation from an ideal semicircular shape. When α = 1, **Equation (10)** corresponds to the impedance of an ideal capacitor, in which case the constant Q becomes equivalent to the capacitance C [38].

For α <1, Bhomik and al. demonstrated that the presence of a constant phase element (CPE) indicates non-Debye-type dielectric relaxation [39]. This behavior is typically associated with a distribution of R–C elements and structural or compositional heterogeneities within material.

To validate the choice of the equivalent circuit, **Figure 6 (c, d)** shows the variations of the experimental values of $Z'$ and $-Z''$ as a function of the simulated values obtained using the parameters extracted from the proposed equivalent circuit at various temperatures. The excellent overlap between experimental and simulated data, characterized by a linear relationship with a slope close to unity at each temperature, confirms that the selected equivalent circuit accurately models the electrical behavior of the investigated compound [40, 41].

Fitted Values ($R_1$, $Q_1$, $\alpha_1$, $C_1$, $Q_2$, and $\alpha_2$) of the equivalent circuit elements are reported in **Table 3**. The capacitances associated with $CPE_1$ and $CPE_2$ occur in the range of $10^{-11}$ F to $10^{-6}$ F which indicate that the high-frequency semicircle corresponds to grain (bulk) contributions, whereas the low-frequency response is related to interfacial effects at the electrode-material interface.

Based on the previous bulk resistance values and the geometric dimensions of the sample, the grain electrical conductivity ($\sigma_{dc}$) at each temperature can be determined using the following equation:

$$\boldsymbol{\sigma_g = \frac{e}{R_1 l}} \qquad (11)$$

Where e and *l* respectively represent the thickness and the surface area of the sample-electrode contact.

The grain conductivity $\sigma_g$ of the $NaMn_2O_4$ sample, measured under a constant applied voltage of 1 V across a temperature range of 303 K to 423 K, is presented in **Figure 6. e**. The plot of Ln ($\sigma_{DC}$ *T) versus 1000/T exhibits a straight line indicating the absence of any phase transition within this temperature interval.

The observed linear increase in DC conductivity with temperature reflects a thermally activated conduction mechanism. As the temperature rises, the number of mobile charge carriers increases due to the additional thermal energy. This behavior suggests thermally assisted hopping or tunneling of charge carriers between localized energy states, in agreement with the Arrhenius-type conduction model [42].

$$\boldsymbol{\sigma_{DC} T = \sigma_0 \exp(-\frac{E_a}{K_B T})} \qquad (12)$$

where T is absolute temperature, $\sigma_0$ is pre-exponential factor, $k_B$ is Boltzmann constant, and $E_a$ is activation energy of the transport process.

Upon linear fitting, we determined the activation energy values for the $NaMn_2O_4$ sample to be $E_a$=0.689(4) eV **(Figure 6. e**).

This value is significantly higher than that reported for $LiMn_2O_4$ ($E_a \approx 0.32$ eV) by Karoui and al. [11], suggesting that charge transport in $NaMn_2O_4$ is more thermally activated, possibly due to stronger carrier localization or structural differences influencing the conduction mechanism.

### III.5. Complex modulus analysis:

The complex modulus formalism was originally introduced by P. B. Macedo et al. [43] as a tool to investigate space charge relaxation phenomena, carrier hopping dynamics, and related processes. One of the main advantages of this representation is its sensitivity to low capacitance contributions, which allows it to effectively minimize the influence of electrode polarization. The electric modulus can be calculated using the following relation [44]:

$$\boldsymbol{M^* = j\omega C_0 Z^* = M' + jM'' = M_\infty \left[1 - \int_0^\infty e^{-i\omega t} \left(-\frac{d\varphi(t)}{dt}\right) dt\right]} \qquad (13)$$

where the real part of modulus is $M' = \omega C_0 Z''$; imaginary part is $M'' = \omega C_0 Z'$ (ω denotes the angular frequency). The capacitance $C_0$ is defined as $C_0 = \frac{\varepsilon_0 e}{l}$, where $\varepsilon_0$ is the permittivity of free space, *e* is the cross-sectional area of the electrode, and *l* is the thickness of the sample. Additionally, φ(t) represents the function that shows the time evolution of the electric field within the materials ($0 \leq \varphi(t) \leq 1$).

**Figure 7.a** illustrates the frequency dependence of the modulus real part (M′) at various temperatures. At low frequencies, M′ exhibits value close to zero, which suggests the absence of a restoring force limiting the mobility of charge carriers under an applied electric field. This behavior reflects long-range charge carrier motion and is typically associated with electrode polarization effects. As the frequency increases, M′ shows a continuous dispersion followed by a tendency to saturate at higher frequencies, reaching an asymptotic maximum. This increase of M′ with frequency, observed at all temperatures, indicates a transition to short-range mobility of charge carriers—particularly ionic species—consistent with localized relaxation processes within the material.

**Figure 7.b** presents the variation of the modulus imaginary part (M″) as a function of frequency at different temperatures. The M″ spectra exhibit well-defined peaks ($M''_{max}$) whose positions shift toward higher frequencies with increasing temperature, indicating that the relaxation processes are thermally activated. This behavior reflects the temperature dependence of the charge carrier dynamics in the material.

At lower frequencies, on the left-hand side of the peak, M″ increases gradually, corresponding to long-range ion mobility where charge carriers—such as $Na^+$ ions—can hop between neighboring sites. Conversely, at high frequencies (right-hand side of the peak), M″ decreases, indicating that the ions are confined to potential wells, allowing only localized or short-range motion. This evolution from long- to short-range mobility with frequency highlights the dispersive nature of the relaxation mechanism [45].

Additionally, the asymmetric broadening of M″ peaks suggest the presence of a distribution of relaxation times, which confirms a non-Debye type relaxation behavior like that observed in other related compounds. The modulus response in this system is well described by the modified Kohlrausch–Williams–Watts (KWW) function as proposed by Bergman. The imaginary part of the electric modulus is defined as [46, 47]:

$$\boldsymbol{M''} = \frac{\boldsymbol{M''_{1\,max}}}{\left((\mathbf{1}-\boldsymbol{\beta_1})+\left(\frac{\boldsymbol{\beta_1}}{\mathbf{1}+\boldsymbol{\beta_1}}\right)\right)\left[\left(\frac{\boldsymbol{\omega_{1\,max}}}{\boldsymbol{\omega}}\right)+\left(\frac{\boldsymbol{\omega}}{\boldsymbol{\omega_{1max}}}\right)^{\boldsymbol{\beta_1}}\right]} \qquad (14)$$

where $M''_{max}$ is the peak maximum, $\omega_{max}$ is the peak frequency of imaginary part of modulus, and β is exponent. The value of β is positioned in the 0–1 range, which reflects the importance of coupling between mobile ions in the conduction process. A good agreement is observed between the experimental data (scattered points) and the theoretical fitting (solid lines), as shown in **Figure 7.b**.

The temperature dependence of the KWW relaxation time ($\tau_{max}$), associated with the conduction process during electrical relaxation, follows an Arrhenius-type behavior described by the relation:

$$\boldsymbol{\tau = \tau_0 exp\left(\frac{E_a}{k_B T}\right)} \qquad (15)$$

where $E_a$ is the activation energy for the relaxation process, $k_B$ is the Boltzmann constant and $\tau_0$ is the pre-exponential factor.

Moreover, the angular frequency corresponding to the relaxation maximum, $\omega_{max}$, also obeys an Arrhenius law:

$$\boldsymbol{\omega_{max} = \omega_0 \exp\left(\frac{-E_a}{k_B T}\right)} \quad (16)$$

where $\omega_0$ is the characteristic pre-exponential factor and $E_a$ is the activation energy.

**Figure 7.c** displays the variation of $Ln(\omega_{max})$ as function of 1000/T. From the slope of the resulting straight line, the activation energy was estimated to be 0.661 eV. This value confirms that the relaxation dynamics are thermally activated and governed by the same energy barrier as that observed for the conduction process, which is primarily driven by the thermally activated motion of monovalent $Na^+$ ions.

### III.6. AC conductivity and conduction mechanism OLPT

To gain a deeper understanding of the electrical transport mechanism and the dynamic behavior of charge carriers in the $NaMn_2O_4$ compound, it is essential to study the AC conductivity as a function of frequency and temperature. This approach enables the differentiation between long-range and localized conduction processes and provides insight into the nature of the relaxation mechanisms involved.

The complex AC conductivity can be described by the relation [48]:

$$\boldsymbol{\sigma^*_{AC}(\omega, T) = \frac{e}{l}\left(\frac{Z^*(\omega)}{(Z'^2 + Z''^2)}\right) = \sigma'_{AC}(\omega) + j\sigma''_{AC}(\omega)} \qquad (17)$$

The real and imaginary parts of the total AC conductivity are respectively given by:

$$\boldsymbol{\sigma'_{AC}(\omega, T) = \frac{e}{l}\frac{Z'}{(Z'^2 + Z''^2)}} \qquad (18)$$

$$\boldsymbol{\sigma''_{AC}(\omega, T) = \frac{e}{l}\frac{Z''}{(Z'^2 + Z''^2)}} \qquad (19)$$

where e and *l* represent the thickness and the cross-sectional area of the sample, while $Z'$ and $Z''$ are the real and imaginary components of the complex impedance.

**Figure 8.a** illustrates the evolution of the real part of AC conductivity, $\sigma'_{AC}(\omega, T)$ at various temperatures. The spectra exhibit two typical features: a frequency-independent plateau at low frequencies, attributed to DC conductivity from long-range ion motion, and a dispersive region at higher frequencies, which is related to the localized hopping of charge carriers between $Mn^{3+}$ and $Mn^{4+}$ ions within $MnO_6$ octahedral. This behavior supports the presence of a thermally activated hopping mechanism and is well described by Jonscher's universal power law [49]:

$$\boldsymbol{\sigma'_{AC} = \sigma_{DC} + A\omega^{s}} \qquad (20)$$

where $\sigma_{DC}$ represents the direct current conductivity in a given temperature range, A is a temperature-dependent pre-exponential factor that reflects the strength of polarizability, and s is a temperature-dependent exponent ranging from 0 to 1. The exponent (s) provides insight into the interaction strength between mobile ions and their surrounding environment and is widely used to identify the dominant conduction mechanism in various materials.

This power-law is described by the Almond-West expression:

$$\boldsymbol{\sigma_{AC}(\omega) = \sigma_{DC}\left(1 + \left(\frac{\omega}{\omega_h}\right)^{s}\right)} \qquad (21)$$

The parameter $\omega_h$ , which marks the onset of the frequency-dependent (dispersive) region, is referred to as the hopping frequency of charge carriers. This frequency shifts toward higher values with increasing temperature, indicating that the hopping mechanism is thermally activated. It can be expressed by the following relation [50]:

$$\boldsymbol{\omega_h = \left(\frac{\sigma_{DC}}{A}\right)^{\frac{1}{s}}} \qquad (22)$$

**Figure 8.b** presents the variation of $Ln(\omega_h)$ as a function of (1000/T), associated with the grain conduction process in $NaMn_2O_4$. The linear evolution reveals Arrhenius-type behavior, with an activation energy of about 0.65 eV. This value is in close agreement with the activation energies obtained from DC conductivity ($E_a$=0.689 eV) and electric relaxation ($E_a$=0.661 eV), confirming that the conduction, relaxation, and hopping mechanisms share a common thermally activated process, likely governed by the migration of $Na^+$ ions through the $MnO_6$ octahedral network.

As illustrated in **Figure 8.c**, the temperature dependence of the exponent (s) which suggests that the Overlapping Large Polaron Tunneling (OLPT) model provides the most appropriate description of the conduction mechanism in our compound over the entire investigated

temperature range. Accordingly, for the OLPT model, the AC conductivity, the jump tunneling distance $R_\omega$ and the frequency exponent s are defined as follows [51-52]:

$$\boldsymbol{\sigma_{ac}(\omega,T)} = \frac{\boldsymbol{\pi^4 e^2 K_B^2 T^2 \alpha^{-1}\, \omega\, [N(E_F)]^2\, R_\omega^4}}{\boldsymbol{12(2\alpha K_B T + \frac{W_{H0} r_p}{R_\omega^2})}} \quad (23)$$

$$\boldsymbol{R_\omega(\omega,T)} = \frac{\boldsymbol{1}}{\boldsymbol{4\alpha}}\left\{\left(\boldsymbol{Ln\left(1/\omega\tau_0\right) - \frac{W_{H0}}{k_B T}}\right) + \left[\left(\boldsymbol{\frac{W_{H0}}{k_B T} - Ln\left(1/\omega\tau_0\right)}\right)^2 + \boldsymbol{\frac{8\alpha W_{H0} r_p}{k_B T}}\right]^{1/2}\right\} \quad (24)$$

and

$$\boldsymbol{S = 1 - \frac{8\alpha R_\omega + \frac{6 W_{H0} r_p}{R_\omega r_p T}}{\left[2\alpha R_\omega + \frac{W_{H0} r_p}{R_\omega K_B T}\right]^2}} \quad (25)$$

where $r_p$ is large polaron radius, α is inverse localization length, $N(E_F)$ is the density of the contained state, $K_B$ is Boltzmann constant, $\tau_0$ is the relaxation time considered as constant of the order of $10^{-13}$ s in various works studied, $W_{H0}$ is activation energy associated with charge transfer between the overlapping sites and $R_\omega$ is the jump tunneling distance.

To evaluate the density of states at the Fermi level $N(E_F)$ and the hopping distance Rω as defined in **Equation (23)**, the temperature dependence of the real part of AC conductivity $\sigma'_{AC}$ at various characteristic frequencies is depicted in **Figure 8.d**. The conductivities decrease linearly with the inverse of the absolute temperature, implying that the AC conductivity is thermally activated. Furthermore, the close agreement between experimental and theoretical values supports the validity of the proposed model, with all relevant parameters summarized in **Table 4**.

The variation of the density of states at the Fermi level, $N(E_F)$, as a function of frequency reveals that increasing frequency leads to a decrease in the polaron radius ($r_p$) and the hopping energy barrier ($W_H$), while $N(E_F)$ increases. This behavior suggests that at higher frequencies, the charge transport is dominated by more localized polarons capable of undergoing faster hopping events over shorter distances and lower energy barriers. Consequently, more localized states become energetically accessible, which explains the increase in $N(E_F)$. **Figure 8.e** illustrates the thermal evolution of the tunneling distance $R_\omega$ for different frequencies. As the temperature rises, $R_\omega$ also increases, indicating that additional thermal energy enables polarons to overcome larger barriers and facilitates inter-site hopping as well as interchain interactions. The values of $R_\omega$ obtained are comparable to the interatomic distances, supporting the notion of localized charge carrier motion. These results suggest that the conduction process in $NaMn_2O_4$ is primarily governed by thermally assisted hopping of $Na^+$ cations along the [001] tunnel

direction, coupled with electron hopping between $Mn^{3+}/Mn^{4+}$ centers in the $MnO_6$ octahedral framework.

## Conclusion

This study highlights the relationship between the structure, optical, and electrical properties of $NaMn_2O_4$ synthesized by the solid-state method. Structural analysis confirms that the compound crystallizes in the orthorhombic system with space group Pnam, and is obtained as a single-phase material. The refined structure reveals two types of manganese ions, $Mn^{3+}$ and $Mn^{4+}$, in a mixed-valence state. The Jahn–Teller distortion observed around $Mn^{3+}$ supports this assignment and influences the charge transport behavior. UV–vis spectroscopy shows that $NaMn_2O_4$ has a direct band gap of about 2.64±0.002 eV, confirming its semiconducting nature and suggesting its potential use in photoelectric and energy storage applications. The absorption bands observed are linked to electronic transitions such as ligand-to-metal and intervalence charge transfer.

Impedance spectroscopy allowed us to model the equivalent circuit and determine the ionic conductivity. The conduction follows the Overlapping Large Polaron Tunneling (OLPT) model, where $Na^+$ ions move through tunnels along the [001] direction, and electrons hop between $Mn^{3+}$ and $Mn^{4+}$ ions. Overall, the combination of mixed-valence manganese, structural tunnels, and Jahn–Teller distortion enables efficient charge transport, making $NaMn_2O_4$ a promising candidate for future energy-related technologies.

## Acknowledgements

The authors extend their appreciation to the Deanship of Research and Graduate Studies at King Khalid University for funding this work through Large Research Project under grant number RGP2/302/46.

## Author contributions

**Marwa Krichen:** writing—original draft, measurements; **Narimen Chakchouk**: data analysis, writing—original draft; **Ebtehal Elghmez**: writing—original draft, funding acquisition; **Fadhel. Hajlaoui**: writing—original draft; **Karim Karoui**: validation, writing—review & editing, funding acquisition.

## Data availability statement

The raw/processed data required to reproduce these findings are available and can be sent if requested.

**Conflict of interest**

The authors declare that they have no conflict of interest.

**References**

[1] Tobias Placke, Richard Kloepsch, Simon Dühnen, Martin Winter,J Solid State Electrochem 21 (2017)1939–1964

[2] Atiyeh Nekahi, Mehrdad Dorri, Mina Rezaei, Mohamed Djihad Bouguern, Anil Kumar Madikere Raghunatha Reddy, Xia Li, Sixu Deng and Karim Zaghib, Batteries 10 (2024) 279

[3] John Abou-Rjeily, Ilham Bezza, Noureddine Ait Laziz, Daniela Neacsa, Cecile Autret-Lambert, and Fouad Ghamouss, ACS Omega 6 (2021) 1064-1072

[4] Yunjia Liu, Muhammad Mitee Ullah, Xiaotong Gao, Peng Liu, Yuqian Li, Wenju Wang, Journal of Power Sources 631 (2025) 236230

[5] Lin Zhu, Hong Wang, Dan Sun, Yougen Tang and Haiyan Wang, J. Mater. Chem. A, 8 (2020) 21387-21407

[6] Kexin Zheng, Haifeng Wang, Jiawei Wang, Zhengqing Pei, Qian Wang, Xinjie Zhou, Dehua Ma, Ju Lu, Haijiao Xie, Ceramics International 51 (2025) 14674-14686

[7] Vaiyapuri Soundharrajan, Balaji Sambandam, Sungjin Kim, Vinod Mathew, Jeonggeun Jo, Seokhun Kim, Jun Lee, Saiful Islam, Kwangho Kim, Yang-Kook Sun, and Jaekook Kim, ACS Energy Lett. 3 (2018) 1998–2004

[8] H. G. Giesber, W. T. Pennington and J. W. Kolis, Acta Cryst. C57 (2001) 329-330

[9] Atiyeh Nekahi, Mehrdad Dorri, Mina Rezaei, Mohamed Djihad Bouguern, Anil Kumar Madikere Raghunatha Reddy, Xia Li, Sixu Deng and Karim Zaghib, Batteries 10 (2024) 279

[10] Junji Akimoto, Junji Awaka, Norihito Kijima, Yasuhiko Takahashi, Yuichi Maruta, Kazuyasu Tokiwa, Tsuneo Watanabe, Journal of Solid-State Chemistry 179 (2006) 169–174

[11] K. Karoui, K. Trabelsi, N. Drissi, Applied Organometallic Chemistry 39 (2024) e7911

[12] Louise Benincasa, Mathieu Duttine, Céline Goujon, Murielle Legendre, Matthew R. Suchomel, Marie Guignard, Inorganic Chemistry 63 (2024) 10373-10385.

[13] Yujun Wu, Wei Shuang, Ya Wang, Fuyou Chen, Shaobing Tang, Xing-Long Wu, Zhengyu Bai, Lin Yang and Jiujun Zhang, Electrochemical Energy Reviews 7 (2024) 17.

[14] Justin C. Hancock, Kent J. Griffith, Yunyeong Choi, Christopher J. Bartel, Saul H. Lapidus, John T. Vaughey, Gerbrand Ceder, Kenneth R. Poeppelmeier, ACS Org. Inorg. Au 2 (2022) 8–22

[15] Xizheng Liu, Xi Wang, Akira Iyo, Haijun Yu, De Li and Haoshen Zhou, J. Mater. Chem. A, 2 (2014) 14822.

[16] Changjian Deng, Paige Skinner, Yuzi Liu, Meiling Sun, Wei Tong, Chunrong Ma, Miu Lun Lau, Riley Hunt, Pete Barnes, Jing Xu and Hui Xiong, Chem. Mater. 30 (2018) 8145−8154.

[17] Alexandros Vasileiadis, Brian Carlsen, Niek J. J. de Klerk, Marnix Wagemaker, chem. Mater. 30 (2018) 6646-6659.

[18] M. Atanasov, J.-L. Barras, L. Benco and C. Daul, J. Am. Chem. Soc. 122 (2000) 4718–4728.

[19] B. Nageswara Rao, O. Padmaraj, D. Narsimulu, M. Venkateswarlu, N. Satyanarayana, Ceramics International, 41 (2015) 14070-14077.

[20] Baskar Senthilkumar, Kalimuthu Vijaya Sankar, Leonid Vasylechko, Yun-Sung Lee and Ramakrishnan Kalai Selvan, RSC Adv., 4 (2014) 53192.

[21] Yongjin Fang, Xin-Yao Yu and Xiong Wen (David) Lou, Matter, 1 (2019) 90-114.

[22] Swagata Dey, Rebecca A. Ricciardo, Heather L. Cuthbert, and Patrick M. Woodward, Inorg. Chem. 53 (2014) 4394−4399.

[23] J.-S. Zhou and J. B. Goodenough, Phys. Rev. Lett. 96 (2006) 247202

[24] J.-S. Zhou and J. B. Goodenough, PHYSICAL REVIEW B 68 (2003) 144406.

[25] E.I. Ross-Medgaarden, I.E. Wachs, J. Phys. Chem. C 111 (2007) 15089–15099.

[26] Moftah Ben Yazid, Moufida Krimi, Abdallah Ben Rhaiem, Amjad Elhams and Ahmed Awhida, African Journal of Advanced Pure and Applied Sciences (AJAPAS), 3 (2024) 277-281.

[27] Khaled Fahmi Fawy, Muhammad Faheem Ashiq, F. F. Alharbi, Sumaira Manzoor, Mehar Un Nisa, Muhammad Ibrahim, Muhammad Tahseen Nawaz Khan, Mouslim Messali, Adeel Hussain Chughtai and Muhammad Naeem Ashiq, Journal of Taibah University for Science 18 (2024) 2302656

[28] Mohammad Allaham, Rashid Dallaev, Daniel Burda, Dinara Sobola, Alois Nebojsa, Alexandr Knápek, Marwan S Mousa and Vladimír Kolařík, Phys. Scr. 99 (2024) 025952.

[29] Martin Ledinsky, Tereza Schönfeldová, Jakub Holovský, Erkan Aydin, Zdeňka Hájková, Lucie Landová, Neda Neyková, Antonín Fejfar and Stefaan De Wolf, J. Phys. Chem. Lett. 10 (2019) 1368–1373.

[30] I. Elhamdi, H. Souissi, O. Taktak, S. Kammoun, E. Dhahri, J. Pina, B.F.O. Costa, E. López-Lago, Heliyon 10 (2024) e29241.
[31] S.M. El-Sayed, G.A.M. Amin, Vacuum 62 (2001) 353-360
[32] Narimen Chakchouk, Dhaifallah R. Almalawi, Idris H. Smaili, Fahad Aljuaid, Abdallah Ben Rhaiem, Applied Organometallic Chemistry 39 (2024) e7871
[33] A. Ajmi, K. Karoui, K. Khirouni and A. Ben Rhaiem, RSC Advances 9 (2019) 14772
[34] M. Ben Bechir and A. Ben Rhaiem, Phys. E 130 (2021) 114686.
[35] A. Bendahhou, P. Marchet, S. E. Barkany and M. Abou-salam, J. Alloys Compd., 882 (2021) 160716.
[36] S. Mathlouthi, A. Oueslati and B. Louati, Indian J. Phys. 93 (2019) 603–610.
[37] T. Rhimi, G. Leroy, B. Duponchel, K. Khirouni, S. Guermazi and M. Toumi, Ionics 24 (2018) 1305–1312.
[38] Mariem Beltaif, Marwa Krichen, Makram Megdiche, Mohamed Dammak,IONICS 25 (2019) 3247-3258.
[39] R.N. Bhowmik, A.G. Lone, J. Alloy. Compd. 680 (2016) 31–42
[40] S. Pandey, D. Kumar, O. Parkash, L. Pandey, Integrat. Ferroelect. 183 (2017) 141–162.
[41] Marwa Krichen, Nidhal Drissi, Karim Karoui, Fathi Jomni, Journal of Molecular Structure 1298 (2024) 137116.
[42] Krichen Marwa and Megdiche Makram, Phys. Chem. Chem. Phys., 27 (2025) 10413.
[43] P. B. Macedo, C. T. Moynihan and R. Bose, Phys. Chem. Glasses 13 (1972) 171.
[44] S. Vinoth Rathan, G. Govindaraj, Materials Chemistry and Physics 120 (2010) 255–262
[45] Bipul Deka, S. Ravi, Journal of alloys and compounds 720 (2017) 589-598
[46] Ahmad Telfah, Mousa M. Abdul-Gader Jafar, Inshad Jum'h, Mais Jamil A. Ahmad, Jörg Lambert, Roland Hergenröder, Polymers for Advanced Technologies, 29 (2018) 1974-1987
[47] S. Nasri, A. L. Ben Hafsia, M. Tabellout and M. Megdiche, RSC Adv., 6 (2016) 76659–76665.
[48] Marwa Krichen, Mohamed Gargouri, Kamel Guidara and Makram Megdiche, IONICS, 23 (2017) 3309–3322
[49] A. K. Jonscher, Nature 267 (1977) 673–679
[50] M. Krichen, M. Megdiche, M. Gargouri and K. Guidara , Indian journal of physics 88 (2014) 1051–1058.
[51] R.K. Panda, R. Muduli, S.K. Kar, D. Behera, Journal of Alloys and Compounds 615 (2014) 899-905
[52] Sudhanshu Kumar, A. K. Shukla and K. Sreenivas, Applied Physics A128 (2022) 381.

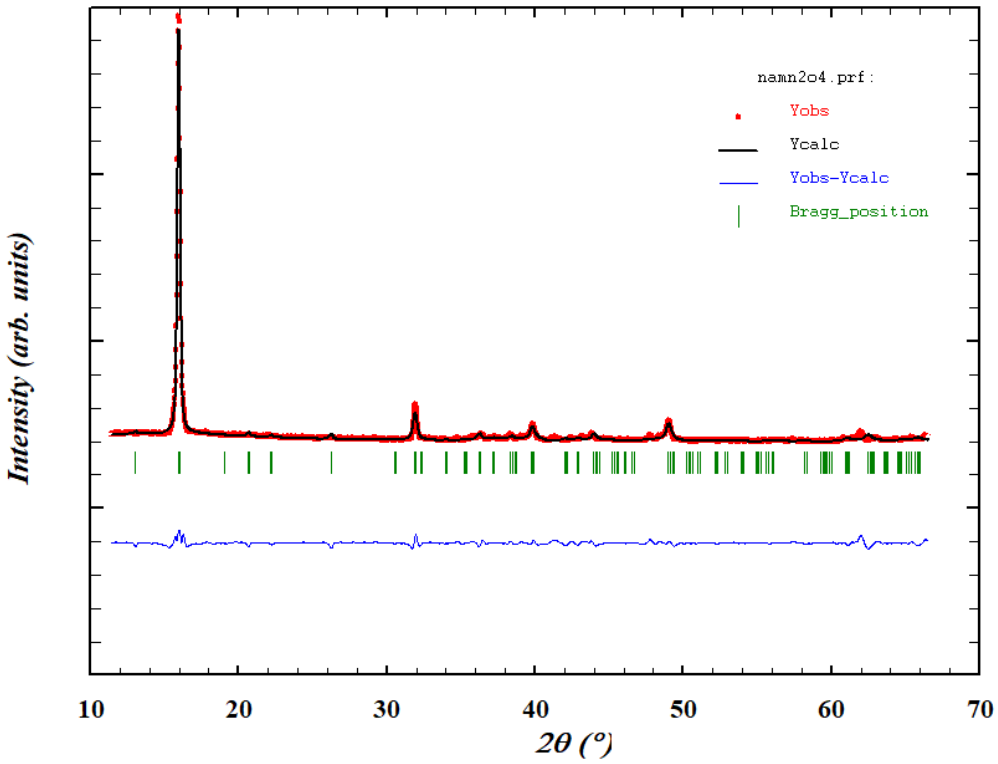


**Figure 1:** Powder X-ray diffraction pattern and Rietveld refinement for the sample $NaMn_2O_4$ (circle signs correspond to experimental data, and the calculated data are represented by the continuous line overlapping them: tick marks represent the positions of allowed reflection, and a difference curve on the same scale is plotted at the bottom of the pattern).

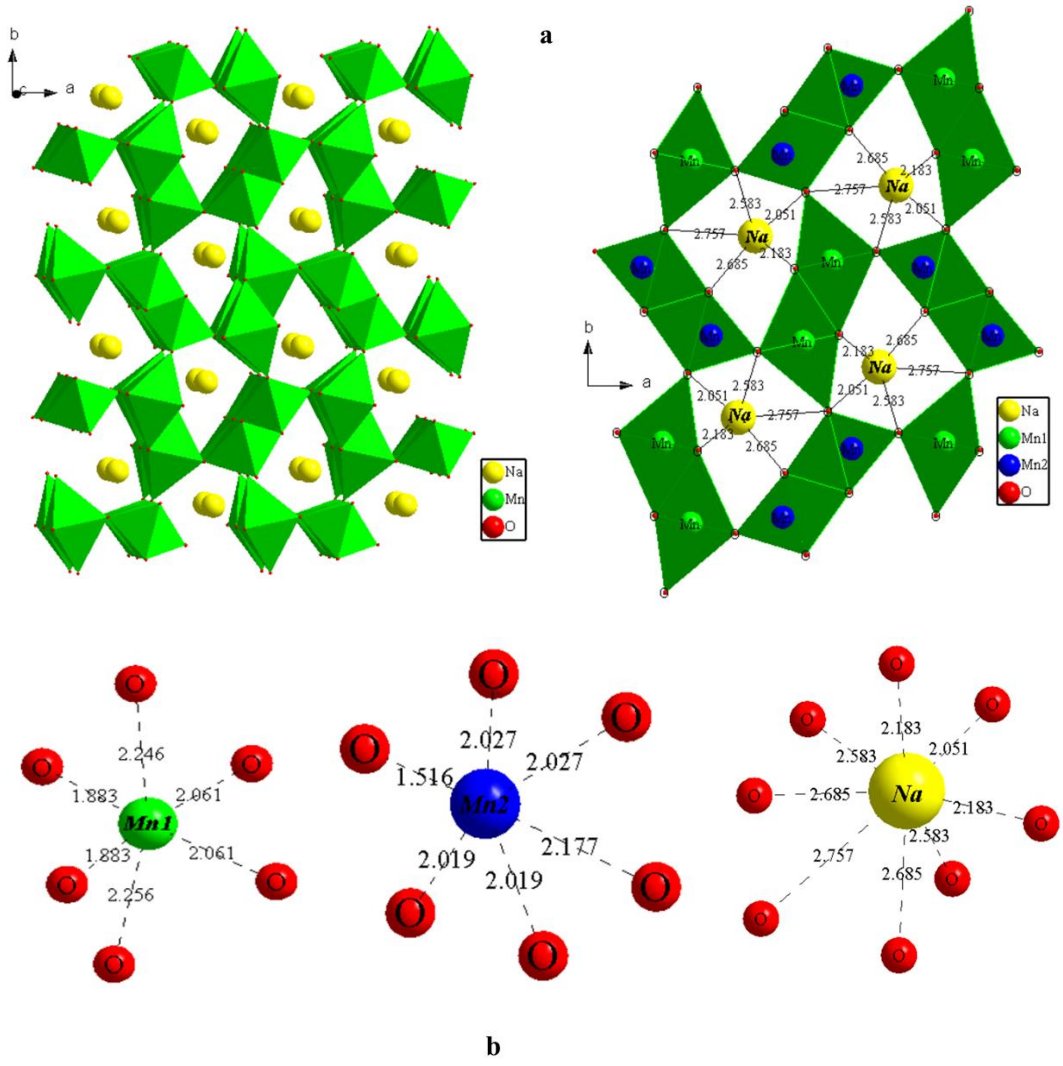


**Figure 2 (a, b)**: The crystal structure **(a)**, polyhedral and interatomic distances **(b)** of $NaMn_2O_4$.

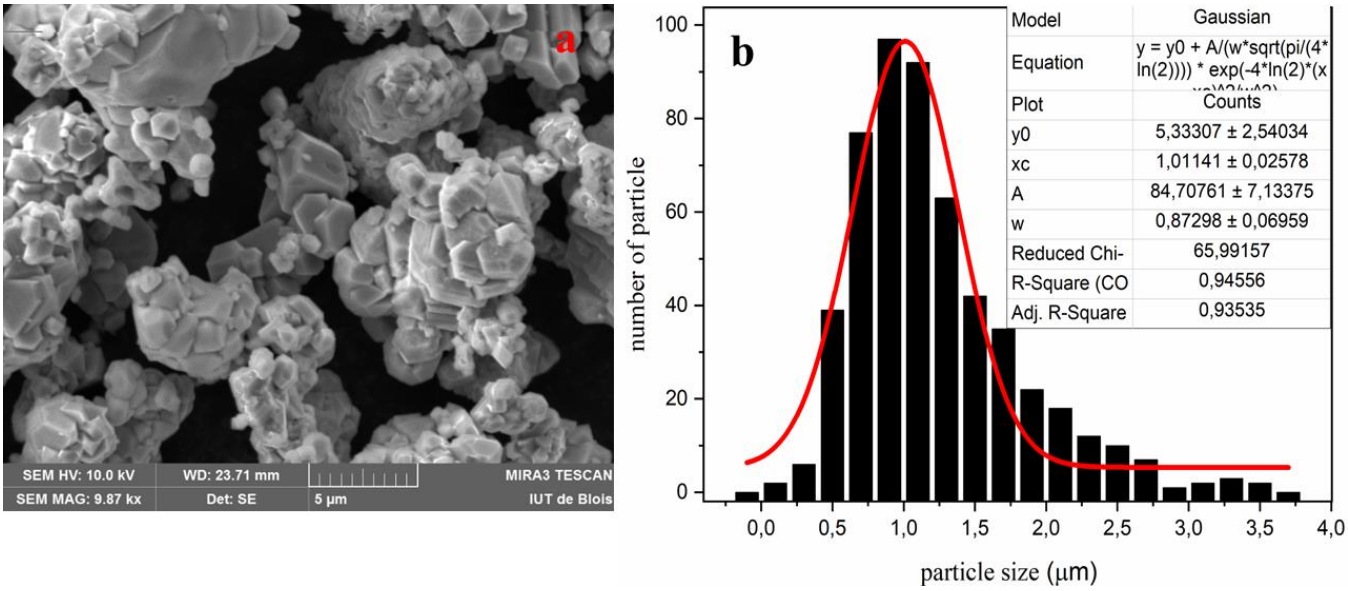


**Figure 3 (a, b):** The SEM picture **(a)** and corresponding particle size histogram **(b)** of $NaMn_2O_4$.

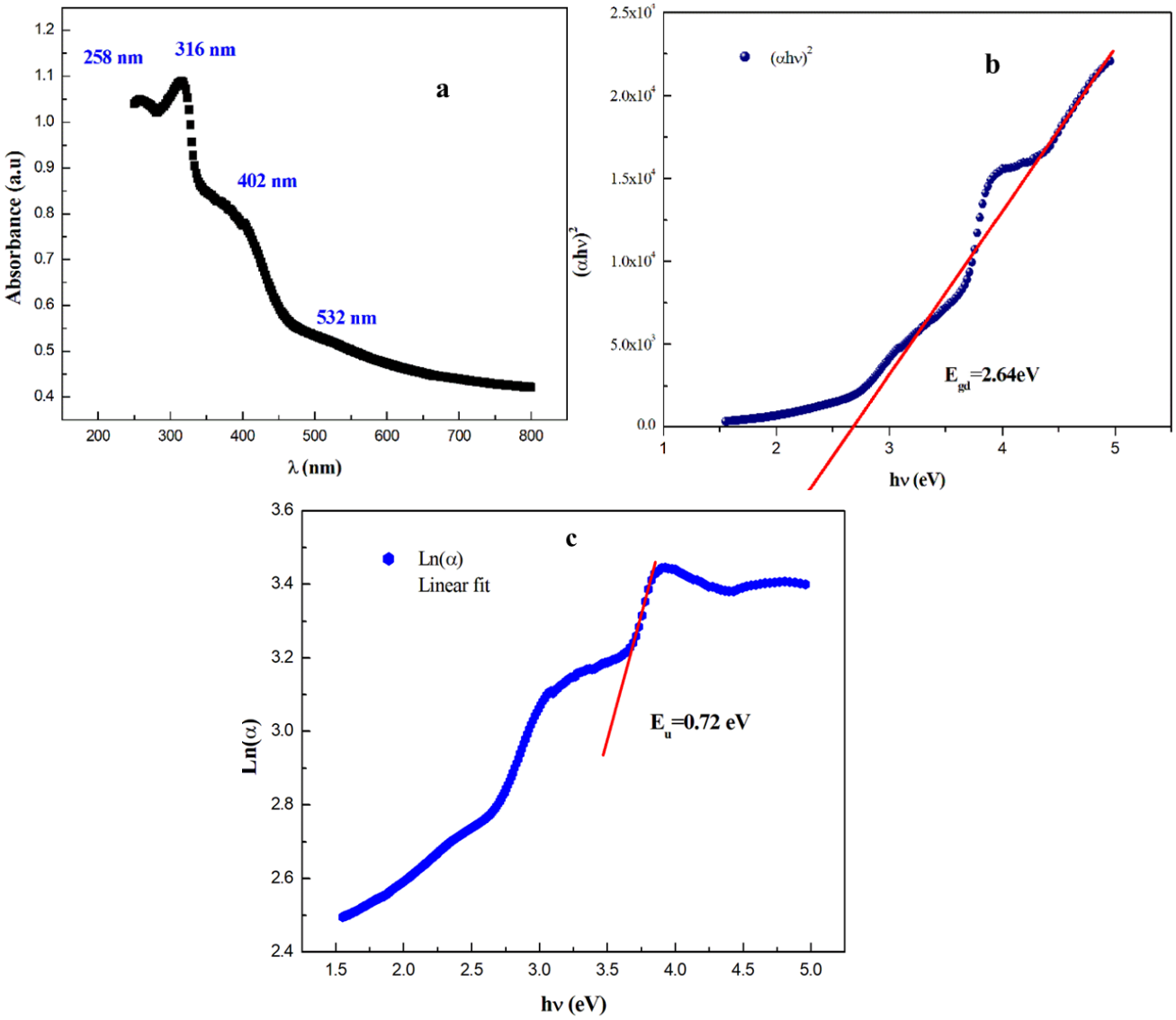


**Figure 4: (a)** Variation of the absorbance wavelength, **(b)** $(\alpha h\nu)^2$ vs hν plots, **(c)** Variation of Ln(α) with Photon Energy (hν) of $NaMn_2O_4$

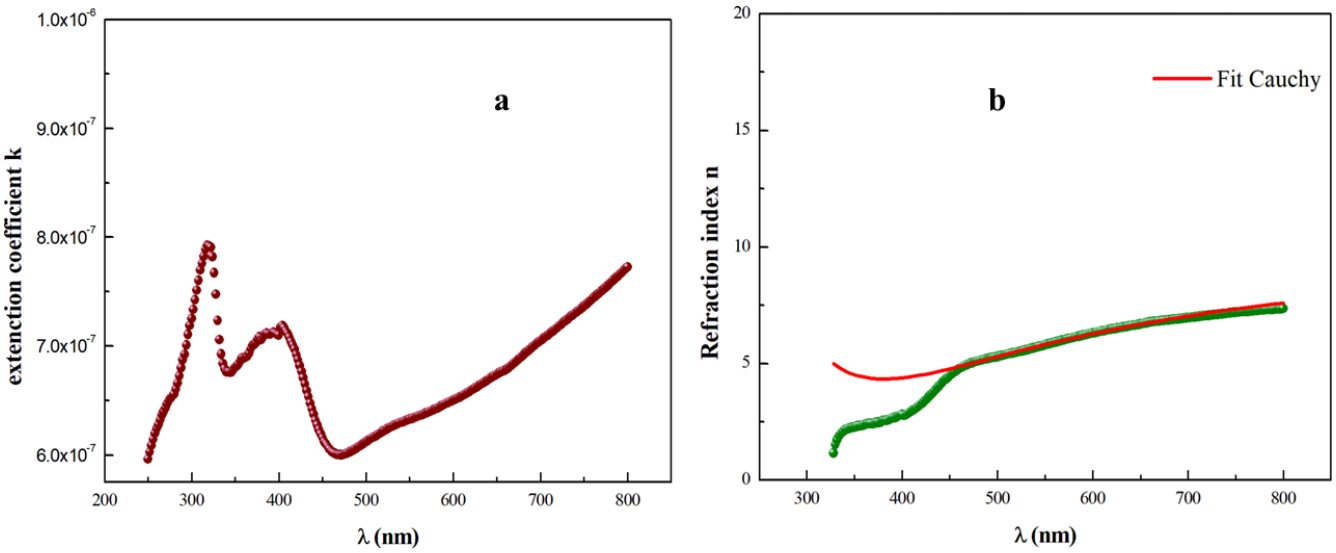


**Figure 5: (a)** Variation of the extinction coefficient K and **(b)** displays the refractive index n wavelength of $NaMn_2O_4$.

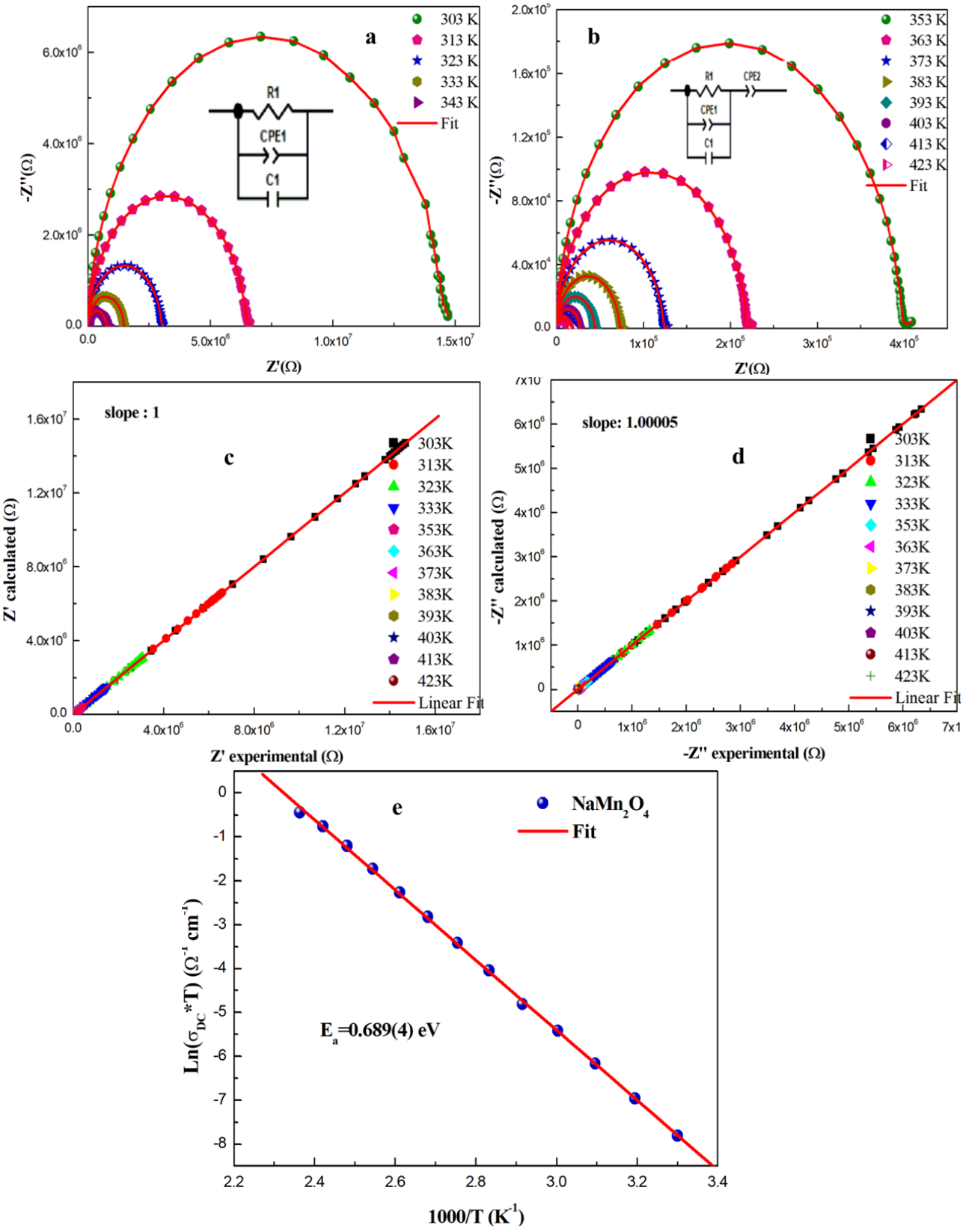


**Figure 6:** Complex impedance spectra in the Nyquist plane with electrical equivalent circuit (inset), accompanied by theoretical data (solid line) for **(a)** low and **(b)** high temperatures**. (c and d)** plots of measured values versus simulated values of the real and imaginary parts of the impedance, **(e)** Variation of the ln (σT) as function of temperature of the $NaMn_2O_4$ sample.

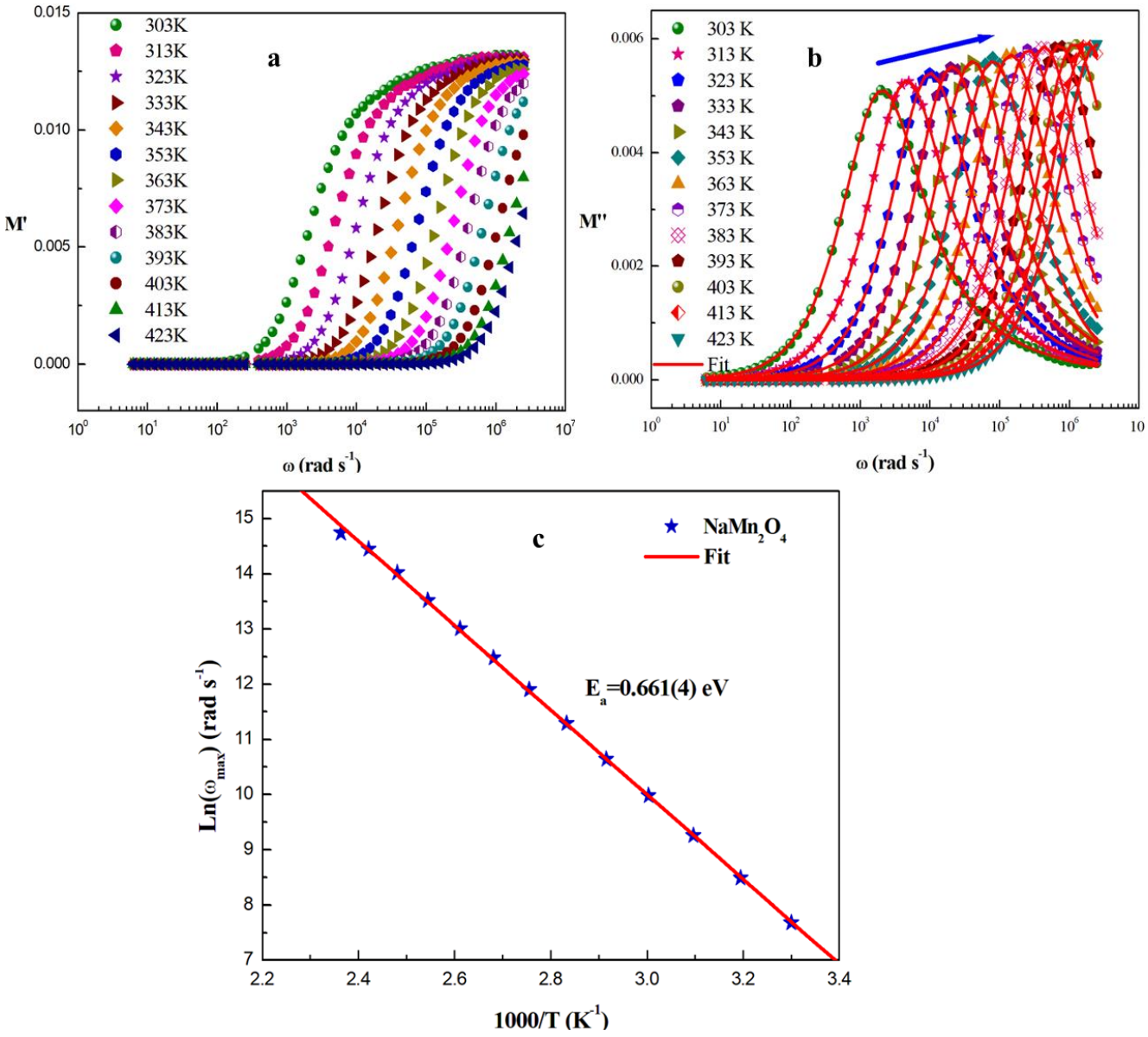


**Figure 7: (a)** Frequency dependence of the real part M′ at different temperatures, **(b)** Angular frequency dependence of the imaginary part M" of electric modulus at several Temperatures, **(c)** The temperature dependence of the conductivity relaxation frequency.

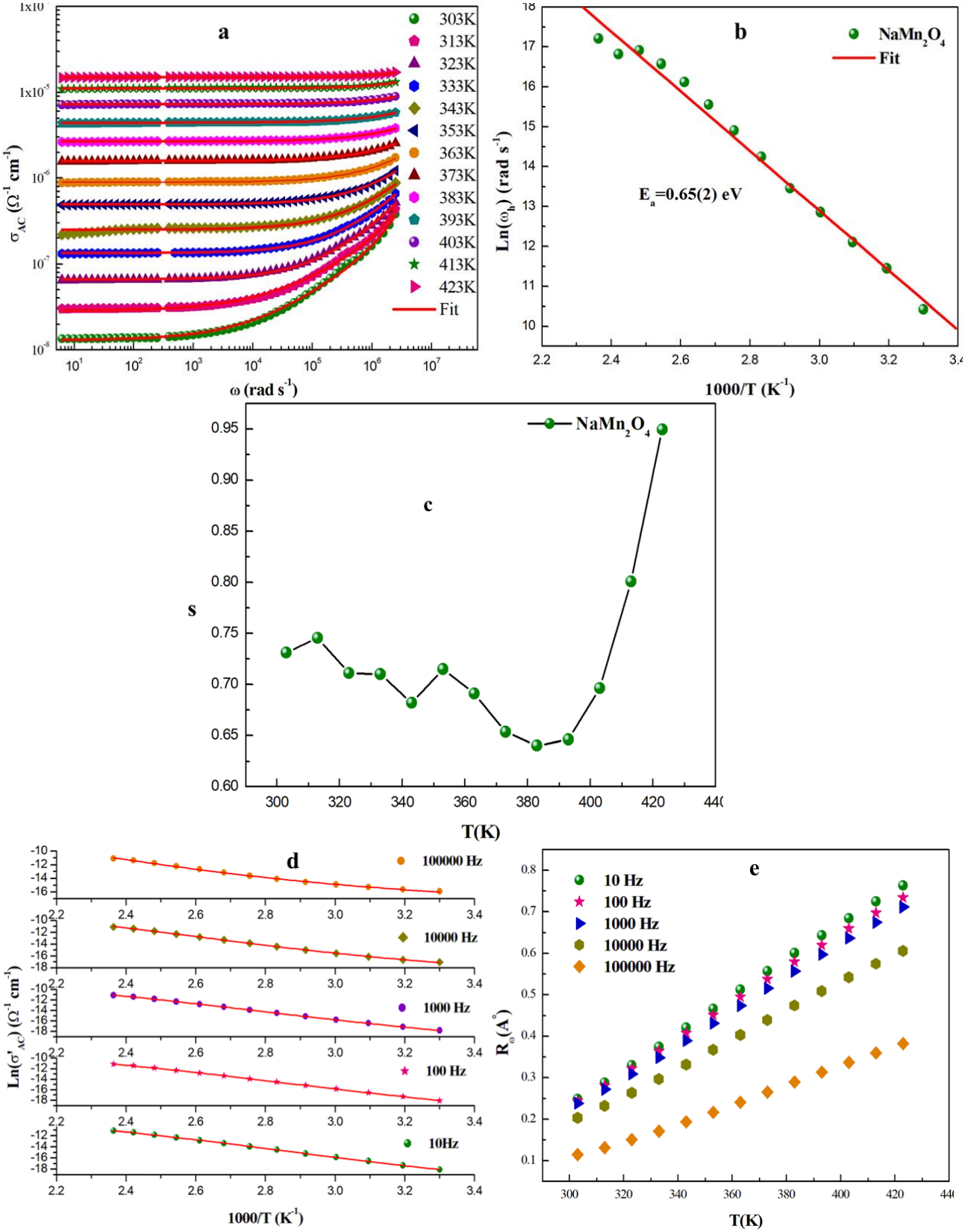


**Figure 8: (a)** Frequency dependence of the real part of AC conductivity at various temperatures, **(b)** Variation Ln($\omega_h$) vs. 1000/T plots, **(c)** Variation for universal exponent s as a function of Temperature, **(d)** Fitting of the real part of AC conductivity at different frequencies using the OLPT model, **(e)** temperature dependence of the tunneling distance $R_\omega$(Å) at different frequencies for $NaMn_2O_4$.

**Table 1:** Crystal data of the $NaMn_2O_4$ (M=Li and Na) compounds.

| samples | $LiMn_2O_4$ [11] | $NaMn_2O_4$ (our study) |
|---|---|---|
| **System** | Cubic | orthorhombic |
| **Space Group** | Fd-3m | Pnam |
| **a (Å)** | 8.1911 | 8.5899 |
| **b (Å)** | 8.1911 | 11.0876 |
| **c (Å)** | 8.1911 | 3.0195 |
| **Volume ($Å^3$)** | 549.57 | 287.58 |
| **Z** | 8 | 4 |
| **$R_p$** | 22.8 | 1.23 |
| **$R_{wp}$** | 15.2 | 1.92 |
| **$R_{exp}$** | 10.3 | 1.52 |
| **Bragg R-Factor** | 1.823 | 1.83 |
| **$R_f$-factor** | 1.556 | 2.65 |
| **$X^2$** | 2.46 | 1.59 |

**Table 2:** Fractional atom coordinates for $NaMn_2O_4$ from X-ray powder diffraction data.

| Atom | x | y | Z |
|---|---|---|---|
| **Na** | **0.28023** | **0.31966** | **0.25** |
| **Mn1** | **0.05062** | **0.11111** | **0.25** |
| **Mn2** | **0.12306** | **0.59428** | **0.25** |
| **O1** | **0.28997** | **0.63867** | **0.25** |
| **O2** | **0.38517** | **0.97351** | **0.25** |
| **O3** | **0.46005** | **0.19794** | **0.25** |
| **O4** | **0.07769** | **0.90961** | **0.25** |

**Table 3:** Refinement parameters for $NaMn_2O_4$ at various temperatures.

| T(K) | $R_1$ ($\times 10^5 \Omega$) | $CPE_1(Q)$ ($\times 10^{-11}$ F) | $CPE_1(\alpha)$ | $C_1$ ($\times 10^{-11}$ F) | $CPE_2(Q)$ ($\times 10^{-6}$ F) | $CPE_2(\alpha)$ |
|---|---|---|---|---|---|---|
| 303 | 148 | 15.1 | 0.674 | 3.23 | | |
| 313 | 65.9 | 18.2 | 0.670 | 3.22 | | |
| 323 | 30.6 | 23.2 | 0.661 | 3.22 | | |
| 333 | 14.9 | 29.1 | 0.654 | 3.23 | | |
| 343 | 8.40 | 18.6 | 0.325 | 3.46 | | |
| 353 | 4.01 | 33.3 | 0.672 | 3.19 | 53.0 | 0.462 |
| 363 | 2.20 | 40.3 | 0.667 | 3.19 | 91.5 | 0.393 |
| 373 | 1.24 | 43.8 | 0.674 | 3.17 | 152 | 0.332 |
| 383 | 0.733 | 36.4 | 0.705 | 3.10 | 247 | 0.292 |
| 393 | 0.441 | 23.9 | 0.759 | 2.95 | 376 | 0.234 |
| 403 | 0.267 | 8.78 | 0.892 | 1.88 | 628 | 0.208 |
| 413 | 0.176 | 9.73 | 0.887 | 1.88 | 953 | 0.252 |
| 423 | 0.131 | 9.30 | 0.893 | 1.88 | 1070 | 0.423 |

**Table 4:** Parameters used for OLPT model fitting in $NaMn_2O_4$.

| **Frequency (Hz)** | $N(E_F)$ (**×10$^{16}$** $eV^{-1}$ $cm^{-3}$) | α ($Å^{-1}$) | $W_{H0}$ (eV) | $r_p$(Å) |
|---|---|---|---|---|
| 10 | 0.993 | 0.192 | 0.676 | 0.669 |
| 100 | 2.57 | 0.203 | 0.615 | 0.604 |
| 1000 | 1.51 | 0.226 | 0.568 | 0.554 |
| 10000 | 4.71 | 0.217 | 0.507 | 0.520 |
| 100000 | 800 | 0.172 | 0.463 | 0.536 |